CHEMISTRY

Marking actinides for separation: Resonance-enhanced multiphoton charge transfer in actinide complexes

Shohei Matsuda[1,2], Keiichi Yokoyama[1]*, Tsuyoshi Yaita[1]*, Tohru Kobayashi[1], Yui Kaneta[2,3], Marie Simonnet[2], Tetsuhiro Sekiguchi[2], Mitsunori Honda[2], Kojiro Shimojo[1], Reisuke Doi[1], Nobuaki Nakashima[4,5]

Precise separation and purification of f-block elements are important and challenging especially for the reduction of nuclear waste and the recycling of rare metals but are practically difficult mainly because of their chemical similarity. A promising way to overcome this difficulty is controlling their oxidation state by nonchemical processes. Here, we show resonance-enhanced multiphoton charge transfer in actinide complexes, which leads to element-specific control of their oxidation states owing to the distinct electronic spectra arising from resonant transitions between f orbitals. We observed oxidation of trivalent americium in nitric acid. In addition, we found that the coordination of nitrates is essential for promoting the oxidation reaction, which is the first finding ever relevant to the primary process of photoexcitation via resonant transitions of f-block elements. The resonance-enhanced photochemical process could be used in the nuclear waste management, as it would facilitate the mutual separation of actinides, such as americium and curium.

INTRODUCTION

Mutual separation among f-block elements is an important technique that should be developed for partitioning of nuclear waste (*1*–*4*), transmutation of harmful nuclides formed in spent nuclear fuels (*5*), and refinement of rare metals for the production of functional materials (*6*), such as strong magnetic materials and long-lived battery for spacecraft (*7*).

The primary difference among those elements is the number of electrons in their f orbitals that belong to the core shell. Therefore, they have similar chemical properties. More specifically, in their most stable states (trivalent states in most cases), they have the same electronic configuration in the valence shell with small differences in the ionic radii and redox potentials. Thus, it is difficult to efficiently separate f-block elements based on their chemical properties. The research on the chemical separation of f-block elements is confronted by many challenges including development of new ligands and electrochemical approaches (*2*, *3*, *6*, *8*–*13*). Among these challenges, we focus on photochemical processes induced by lasers because those photons can be expected to be a powerful tool for the precise separation owing to their ultimately ordered states, i.e., extremely narrow energy spread, and, furthermore, can be regarded as a reagent that never becomes secondary waste. This feature is important especially in the nuclear waste management.

Donohue (*14*, *15*) proposed a smart solution to overcome this difficulty by using the photoredox reaction through resonant f-f transitions. Owing to the difference in the core electron configurations, each element has distinct f-f transition spectra composed of isolated narrow absorption bands like atomic lines even in the liquid phase (*16*–*19*), as shown in Fig. 1 (A and B). This spectroscopic property could be a powerful tool for mutual separation.

However, Donohue did not observe any photoredox reaction despite having tuned the laser to the resonant wavelength of the f-f transitions of some lanthanides. It was reported that the photoredox reaction needs excitation to the charge transfer state (f-d transition). This means that subsequent excitation must follow the initial f-f transition (*20*). To realize such a multistep excitation while suppressing other decay processes, such as luminescence and nonradiative decay, high photon density is required. Strong, short laser pulses need to be tightly focused without inducing breakdown due to the ionization of solvent molecules or substrates. Yamada and Ohno (*21*) tried to observe the process by focusing a laser onto a europium chloride crystal. However, only nonresonant two-photon reduction was observed without any evidence of resonant f-f transitions.

Nakashima and co-workers (*22*) demonstrated multiphoton reduction of trivalent europium through one of its f-f transitions with careful tight focus. They also reported the reduction of trivalent ytterbium and samarium (*23*, *24*). For other lanthanides, no process has been reported so far. This is probably because only these three lanthanides can take stable divalent states in aqueous solutions.

Unlike lanthanides, actinides take several oxidation states in solution, although the most stable one is still trivalent after americium. For example, they take pentavalent or hexavalent states by forming double bonds with two oxygen atoms, like $U^{VI}O_2^{2+}$ and $Am^{V}O_2^{+}$. Actually, photoreduction of $U^{VI}O_2^{2+}$ was extensively studied for separation (*25*–*28*), although it was a one-photon process without any f electrons involved. On the other hand, a multiphoton process involving f-f transitions has not been demonstrated so far. Such a demonstration may give new insight into nuclear waste management by aiding the mutual separation of actinides.

First, we report observation of the resonance-enhanced photochemical process involving actinides, where trivalent americium coordinated to nitrate ions was oxidized to pentavalent americium because of the photoexcitation at 503 nm. Second, using solvent extraction, we demonstrate photochemical separation of americium

[1]Materials Sciences Research Center, Japan Atomic Energy Agency, 1-1-1 Kouto, Sayo-cho, Sayo-gun, Hyogo 679-5148, Japan. [2]Materials Sciences Research Center, Japan Atomic Energy Agency, 2-4 Shirakata, Tokai-mura, Naka-gun, Ibaraki 319-1195, Japan. [3]Department of Chemical Science and Engineering, Graduate School of Engineering, Kobe University, 1-1 Rokkodai, Nada, Kobe, 657-8501, Japan. [4]Department of Chemistry, Graduate School of Science, Osaka City University, 3-3-138 Sugimoto, Sumiyoshi-ku, Osaka 558-8585, Japan. [5]Institute for Laser Technology, 1-8-4 Utsubo-honmachi, Nishi-ku, Osaka 550-0004, Japan.
*Corresponding author. Email: yokoyama.keiichi@jaea.go.jp (K.Y.); yaita@spring8.or.jp (T.Y.)

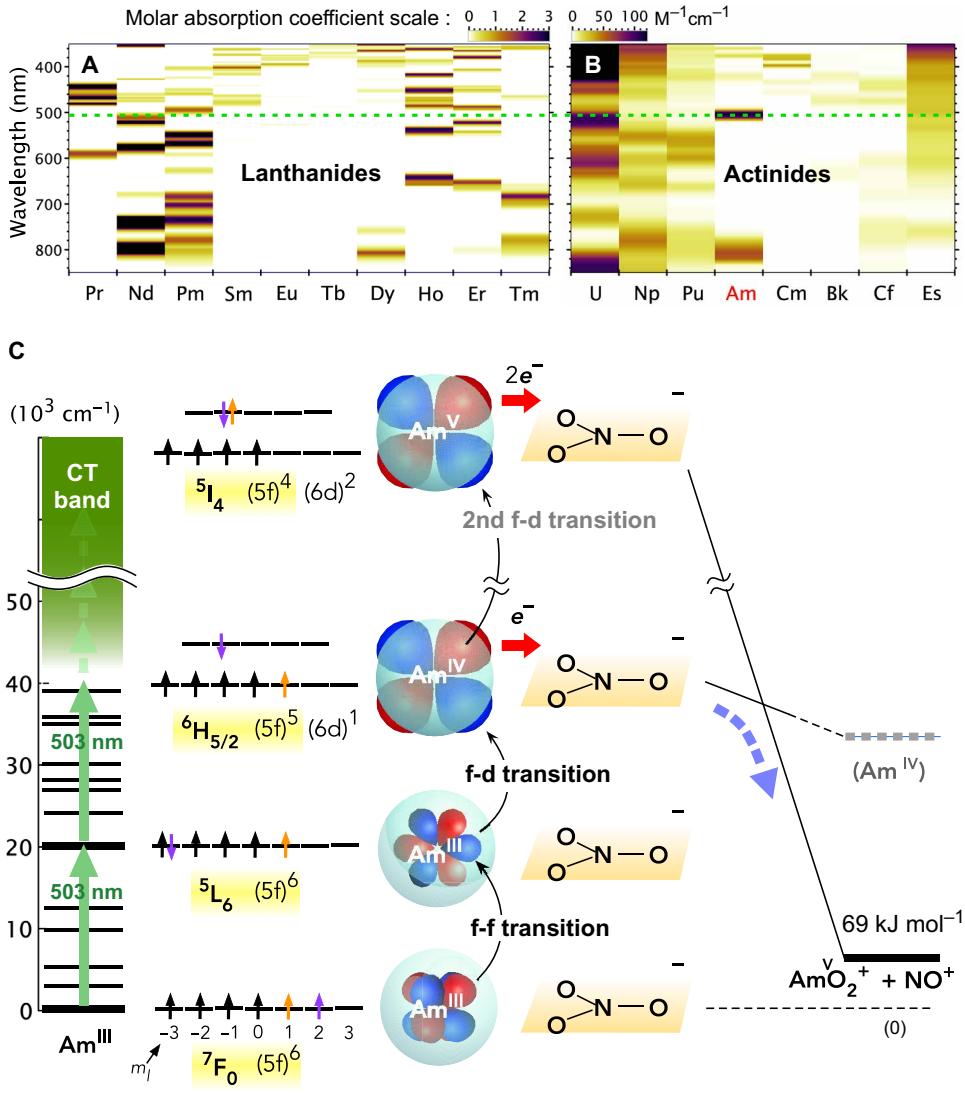

Fig. 1. Concept and mechanism of the resonance-enhanced multiphoton oxidation. (**A** and **B**) UV/vis (visible) spectra of some trivalent lanthanides and actinides in solutions [digitized from figures 3 and 5 (neither capitalizing nor coloring) of (*17*) and figure 3 of (*18*)]. The green dashed line indicates the laser wavelength to be tuned to select americium. (**C**) Image of the oxidation mechanism discussed in this study. Atomic orbitals of americium are depicted to visually reveal the promoted electron (also indicated by purple or orange arrows in the configuration diagrams) but not to present theoretically correct pictures of the orbitals. Given electron configurations of each state of atomic americium are shown. Each configuration diagram represents one of the degenerating configurations. Term symbols do not take into account the electron configurations of 6d orbitals. Electronic energy diagram of trivalent americium depicted on the left-hand side is obtained from the absorption peaks reported by Carnall (*18*, *19*). The continuous absorption band above 42,500 cm^{-1} is attributed to a charge transfer (CT) band (*39*).

from lanthanide as well as Donohue did that of europium with one-photon reduction using broad charge transfer band in the ultraviolet (UV) region (*29*). Third, we discuss the mechanism on the basis of nitrate activity dependence of the oxidation rate and the geometry of the coordination complex (Fig. 1C).

RESULTS

By tightly focusing 503-nm laser pulses, we observed the depression of the sharp absorption band at 503 nm assigned to an f-f transition of trivalent americium (*30*–*33*) and simultaneous growth of the 717-nm band attributed to that of pentavalent americium (*30*, *34*, *35*) as shown in Fig. 2A, indicating occurrence of photooxidation of trivalent americium. There is no evidence for the formation of hexavalent americium, $Am^{VI}O_2^{2+}$, whose spectral feature should appear at 666 nm (*30*, *31*, *35*, *36*). The pentavalent state has survived for weeks without substantial reverse reaction, implying that the formed pentavalent species must be $Am^{V}O_2^{+}$, which is a metastable species of pentavalent americium. In addition, two peaks in the UV region are assigned to nitrous acid, HNO_2 (Fig. 2A) (*37*). Nitrous acid has vanished in a week.

To demonstrate the separation of actinides from fission products using photooxidation, we added trivalent praseodymium for a practical reason stated in the "Experimental methods" section in Materials and Methods. We conducted a solvent extraction experiment with TODGA (*N*,*N*,*N*′,*N*′-tetraoctyl-3-oxapentanediamide)/dodecane

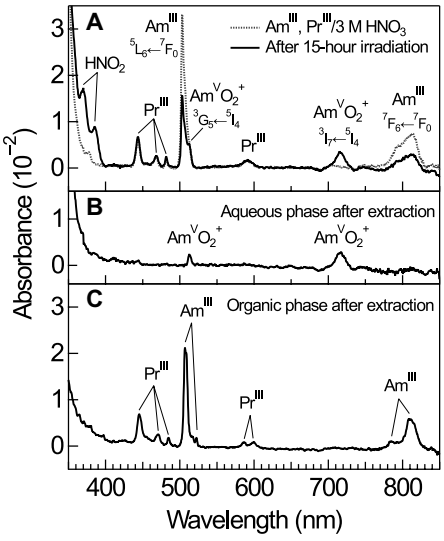

Fig. 2. Effect of laser irradiation and solvent extraction on absorption spectra of sample solutions. (**A**) Absorption spectrum of 0.1 mM Am^{III} and 0.55 mM Pr^{III} in 3 M HNO_3 solution before (gray dotted line) and after 15-hour laser irradiation at 503 nm with laser pulse energy of ~30 mJ (black solid line) with the spectral band width of 1 nm. Peaks at 503 and 800 nm are assigned to the $^5L_6 \leftarrow {}^7F_0$ and $^7F_6 \leftarrow {}^7F_0$ transitions of trivalent americium, respectively (*30*–*33*). Peaks at 444, 468, 482, and 590 nm are assigned to trivalent praseodymium (*38*). Peaks at 513 and 717 nm are assigned to the $^3G_5 \leftarrow {}^5I_4$ and $^3I_7 \leftarrow {}^5I_4$ transitions of pentavalent americium, respectively (*30*, *34*, *35*). The two peaks in the UV region are assigned to nitrous acid (HNO_2). (**B** and **C**) Aqueous (B) and organic (C) phase spectra measured with the spectral band width of 1 nm after extraction of trivalent species by 16 mM TODGA in dodecane from the irradiated sample solution.

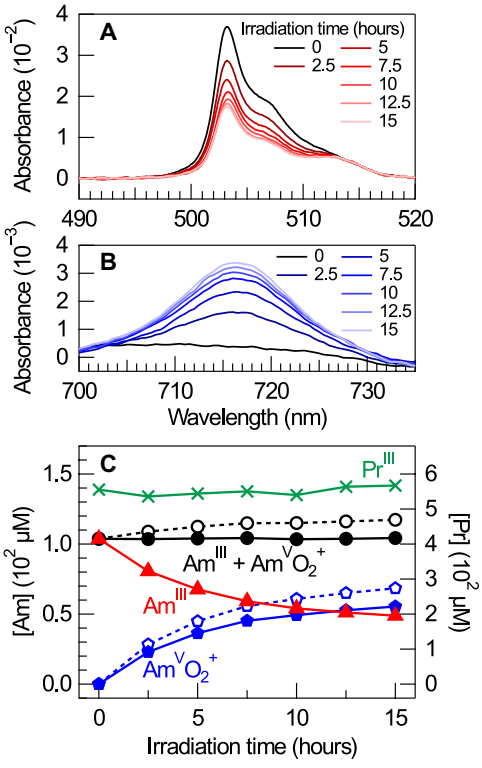

Fig. 3. Evolution of the absorption peaks and derived concentrations. (**A** and **B**) Evolutions of the Am^{III} absorption in the region of 490 to 520 nm measured with a spectral bandwidth of 0.2 nm (A) and the $Am^{V}O_2^+$ absorption in the region of 700 to 735 nm measured with a spectral bandwidth of 1 nm (B). (**C**) Concentration of americium and praseodymium as a function of laser irradiation time. Concentration is obtained from observed absorbance and reported value of molar absorption coefficient. Triangle, open pentagon, open circle, and cross mark stand for concentrations of trivalent, pentavalent, and total americium and of trivalent praseodymium, respectively. Closed pentagon represents the concentration of pentavalent americium calculated with the molar absorption coefficient adjusted so as to let the alteration of the total concentration of americium ($[Am^{III}] + [Am^{V}O_2^+]$) be minimized. Closed circle represents the total concentration with the adjusted concentration of $Am^{V}O_2^+$.

from the irradiated solution after 1 week of storage. After the extraction, the photochemical product, $Am^{V}O_2^+$, remained in the aqueous phase (Fig. 2B), whereas trivalent species were transferred to the organic phase (Fig. 2C). As a result, we obtained almost pure $Am^{V}O_2^+$ aqueous solution and a mixture of Am^{III} and Pr^{III} in the organic phase. This preliminary result implies that we can clearly separate americium from fission products and other trivalent minor actinides if conversion ratio of the photooxidation approaches 100%.

Figure 3 (A and B) shows the evolution of spectra for Am^{III} (Fig. 3A) and $Am^{V}O_2^+$ (Fig. 3B) during the 15-hour irradiation. We observed the gradual depression and growth of trivalent and pentavalent americium, respectively. Although the absorbance at ~513 nm in Fig. 3A seems unchanged, that is because the $Am^{V}O_2^+$ spectrum is superimposed. To check the mass balance between Am^{III} and $Am^{V}O_2^+$, we calculated their concentrations on the basis of reported molar absorption coefficients (*31*). The concentration was plotted as a function of laser irradiation time (Fig. 3C). Apparently, the decrease in $[Am^{III}]$ and the increase in $[Am^{V}O_2^+]$ are balanced. However, the total concentration of americium, $[Am^{III}] + [Am^{V}O_2^+]$, gradually increases with increasing irradiation time. It is not acceptable that the total concentration exceeds the initial value. Hence, we determined a recommended value of molar absorption coefficient of $Am^{V}O_2^+$ at 717 nm as 54 M^{-1} cm^{-1}, so as to keep the total concentration constant. Aside from checking by mass balance, the selectivity of the photooxidation is confirmed by the observation of an almost constant praseodymium concentration, as obtained from the spectral peak at 444 nm with reported molar absorption coefficient (*38*). These results support that Am^{III} is converted exclusively into $Am^{V}O_2^+$ with a high selectivity, proving the applicability of this method to an actual separation process by tightly focusing laser pulse at 503 nm.

To clarify the mechanism of the photooxidation of trivalent americium, we investigated laser wavelength, laser fluence, and nitrate activity dependence of the instantaneous rate of the photooxidation without praseodymium. Typical results of an experiment for this purpose are shown in fig. S1 (A to D). These were similar to the above experiment including Pr^{III}. The amount of depression at the 503-nm band was proportional to the laser irradiation time but negligibly small compared with the initial integrated intensity of the band in the case of sufficiently short irradiation time. Thus, in subsequent analyses, we used a pseudo–first-order rate constant to make the results comparable between different irradiation duration and initial concentrations of trivalent americium (see the "Pseudo–first-order rate constant" section in Materials and Methods).

Oxidation was observed only when the laser was tuned to a wavelength within the 503-nm band (Fig. 4A). The largest rate constant

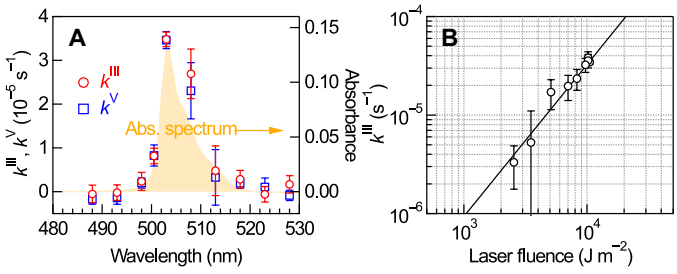

Fig. 4. Wavelength and fluence dependence of the rate constant. (**A**) Laser wavelength dependence of the rate constant obtained from the depression at 503 nm (red circle) and growth at 717 nm (blue square) plotted together with the absorption spectrum of trivalent americium (yellow area). These data were obtained with a laser pulse energy of ~32 mJ at [HNO_3] = 3 M. Error bar denotes 1σ, i.e., SD. (**B**) Laser fluence dependence of the rate constant obtained from the depression at 503 nm plotted together with a fitted line with a single exponent. These data were obtained at [HNO_3] = 3 M. Error bar denotes 1σ.

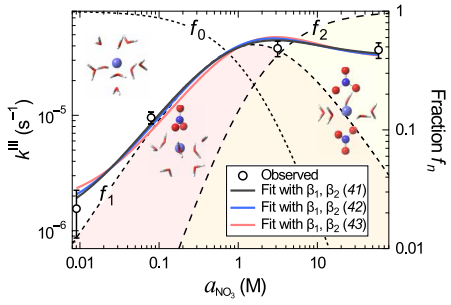

Fig. 5. Nitrate dependence of the rate constant and the number of nitrates in a complex. Observed rate constants for the first-order decay of the 503-nm peak are plotted by open circles together with the best fit curve calculated by Eq.11 with reported stability constants (*41*–*43*) plotted by solid lines. Error bar denotes 1σ. Laser pulse energy was ~32 mJ. For the fit function, Eq. 11 is truncated by the second order in the activity. All of these plots refer to the left axis. The broken lines tagged with letters f_0, f_1, and f_2 referring to the right axis give composition ratio of the complexes, which contain 0, 1, and 2 nitrates, respectively. The fraction is defined by $f_n = [Am^{III}(NO_3)_n]^{3-n}/\sum_{i=0}^{2}[Am^{III}(NO_3)_i]^{3-i}$ ($n = 0$ to 2). The stable structure for each complex is obtained by density functional theory calculations described in the "DFT calculations" section in Materials and Methods.

was recorded at the peak of the band. These results indicate that the oxidation process is triggered by the f-f transition. Notably, the values of k^{III} calculated from the depression at 503 nm using Eq. 10 (in the "Pseudo–first-order rate constant" section in Materials and Methods) and k^{V} from the growth at 717 nm using Eq. 15 (in the "Pseudo–first-order rate constant section" in Materials and Methods) agree well within uncertainties (Fig. 4A), further indicating that the pentavalent state is the dominant product of the photoredox reaction of trivalent americium.

The laser fluence dependence of the rate constant fits better in the logarithmic plots with a slope of 1.5 rather than 1 (Fig. 4B), indicating that at least two photons are needed to trigger the oxidation. Actually, the total energy given by two 503-nm photons is 39,761 cm^{-1}, which is comparable to the lower threshold of the charge transfer band (42,500 cm^{-1}) (*39*) as shown in Fig. 1C.

In general, a two-photon process can be either resonant or nonresonant. The former is a sequence of two single-photon processes mediated by an intermediate state with a finite lifetime. The latter proceeds without formation of such an intermediate and directly forms the final state. This process can be modeled with a virtual intermediate having an infinitely short lifetime, i.e., extremely broad spectrum due to the uncertainty principle. The present observation that the wavelength dependence faithfully follows the profile of one photon absorption spectrum to the $^5L_6$ state (Fig. 3) indicates a resonant process via the real state. Since no oxidation has been observed in the spectral region outside the absorption profile, the present photo process can be regarded as a resonance-enhanced multiphoton charge transfer, which is an analogy to the resonance-enhanced multiphoton ionization.

Figure 5 shows that the rate constant depends on the concentration or activity of nitrate a_{NO3}. The activity is obtained from the stoichiometric concentration of nitric acid at 0.01, 0.1, 3, and 12 M [table 4 in (*40*)]. We observed a linear dependence with a slope of approximately 1 in the lower asymptotic region of $a_{NO3} < 0.1$ M and a saturating curve in the higher asymptotic region ($a_{NO3} > 3$ M). The observed a_{NO3} dependence suggests that the photooxidation would occur not from free (just hydrated) americium but its complexes with nitrates. To quantitatively evaluate the contribution of the two-nitrate complex to the rate constant, the nitrate dependence was fitted with an analytical expression, Eq. 11 (in the "Pseudo–first-order rate constant" section in Materials and Methods), derived from the model of the reaction scheme in Fig. 6, taking $n = 0$, 1, and 2. Equilibrium fractions of their complexes were calculated by each of three pairs of stability constants β_n adapted from the literature (*41*–*43*). By adjusting three specific rate constants k_n in Eq. 11, the nitrate dependence was well reproduced (Fig. 5). For any pair of the stability constants, k_0 is much smaller than k_1, and k_2 is about one-half of k_1. To make this discussion more quantitative, we averaged the ratios of the specific rate constants k_0/k_1 and k_2/k_1 over the three pairs. We obtained $k_0/k_1 = 0.0040 \pm 0.0003$ and $k_2/k_1 = 0.44 \pm 0.07$. The k_0/k_1 ratio means that the photooxidation rate constant of $Am^{III}NO_3^{2+}$ is three orders of magnitude larger than that of free Am^{III} (just hydrated americium). This strongly suggests that a one-nitrate complex is required for the observation of the photochemical process. The k_2/k_1 ratio means that the photooxidation rate constant of $Am^{III}(NO_3)_2^{+}$ is smaller than that of $Am^{III}NO_3^{2+}$. This indicates that the photooxidation is not enhanced by the two-nitrate complex. We conclude that the coordination of single nitrate is critically important in promoting oxidation, and the two-nitrate complex does not accelerate but suppresses the oxidation rate. Since these results are largely affected by the adapted stability constants, we confirmed their reliability by extended x-ray absorption fine structure (EXAFS) analyses (Figs. 7 and 8 and fig. S2).

To estimate k_0, k_1, and k_2 by fitting the nitrate dependence, we used the stability constants, β_1 and β_2, adapted from the literature (*41*–*43*) as mentioned above. Since most of them were measured in the presence of a substantial amount of perchlorate, we discuss the validity of the reported value of the stability constant to the present simple nitrate system. Thus, we focus on the number of nitrates coordinated by the americium N_{NO3}, comparing the value of N_{NO3} calculated from the stability constants with that obtained from the EXAFS analyses in the simple nitrate system. We conducted EXAFS analyses for trivalent neodymium instead of radioactive americium (Fig. 7 and table S1 for K-edge, and fig. S2 and table S2 for L_3-edge). Several features in the radial structure functions (RSFs) are quite similar to those observed in americium (*44*). For example, (i) the first peak

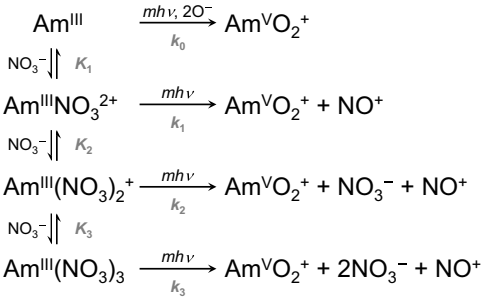

Fig. 6. Reaction scheme modeled for the analysis of photooxidation of trivalent americium in the presence of nitrates. Stepwise coordination of trivalent americium to nitrates is shown in the left-hand side column with respective equilibrium constants K_n. The photooxidations of trivalent americium to the pentavalent state are expressed by right arrows with rate constants k_n. m stands for the number of photons ($m = 2$ or 3). Note that, in the first line, photo oxidation of hydrated Am^{III} requires two O^- from the water molecules to produce $Am^{V}O_2^+$ and $4H^+$.

appears at 2.0 Å; (ii) the first peak profile is well reproduced with solely the oxygen atoms of nine water molecules at the low nitric acid concentration ([HNO_3] < 0.1 M); (iii) the peak profile observed at higher nitric acid concentration contains, more or less, an additional contribution from the contacting oxygen(s) and the nitrogen of the nitrate; and (iv) the small peak observed in the range of 3.5 to 4.0 Å is attributed to multiple scattering via the terminal oxygen and nitrogen in the nitrate of bidentate coordination. By fitting RSFs with these scattering contributions, the numbers of coordinated nitrates are estimated to be $N_{NO3} = 1$ and 2 in the nitric acid concentration [HNO_3] = 3 and 6 M, respectively, for L_3-edge EXAFS and $N_{NO3} = 0.5$, 1, 1.5, and 2 at [HNO_3] = 1, 3, 6, and 12 M, respectively, for the K-edge EXAFS. They are plotted in Fig. 8 with N_{NO3} derived from the EXAFS spectra of the americium nitrate complex (*44*). The good agreement between the EXAFS data for both americium and neodymium and the simulated curves validates the application of stability constants from the literature (*41*–*43*) to the present simple nitric acid solution.

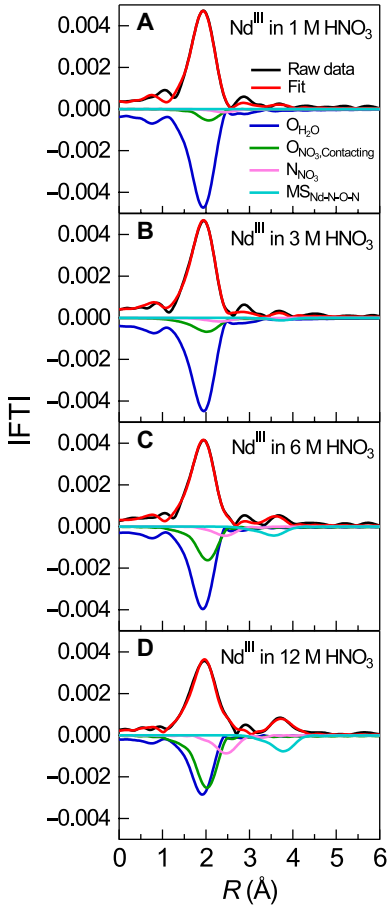

Fig. 7. K-edge EXAFS analyses of neodymium in nitric acid solution. (**A** to **D**) RSF with the best fits and their deconvolutions. RSF functions were obtained by Fourier transform of Nd^{III} K-edge k^3-EXAFS spectra at [Nd^{III}] = 50 mM in 1 M (A), 3 M (B), 6 M (C), and 12 M HNO_3 (D). Solid black and dotted red lines show raw data and fitting curve, respectively. Contributions of scattering pathways from O_{H2O} (blue), $O_{NO3,\ Contacting}$ (green), N_{NO3} (pink), and multiple scattering ($MS_{Nd-N-O-N}$, cyan) are plotted inversely. Optical path length is 20 mm.

DISCUSSION

Here, we discuss possible mechanisms of the formation of pentavalent americium. We observed that (i) a single nitrate must be coordinated for the oxidation, (iii) the two-nitrate complex does not accelerate the oxidation, and (iii) nitrous acid is formed. Two mechanisms satisfying the above three observations are speculated. One is the simultaneous formation of two Am-O bonds, that is, the direct formation of the pentavalent americium accompanied by nitrosonium formation, expressed as follows

$$Am^{III}NO_3^{2+} \xrightarrow{mh\nu} Am^{V}O_2^{+} + NO^{+} (m = 2 \text{ or } 3) \quad (1)$$

$$NO^{+} + H_2O \rightarrow HNO_2 + H^{+} \quad (2)$$

The enthalpy for reaction 1 is estimated to be 69 kJ mol^{-1} from reported enthalpies of formation $\Delta_f H$ (Am^{III}, aq) = −616.7 ± 1.5 kJ mol^{-1} (*45*), $\Delta_f H$ (NO_3^-, aq) = −205.00 kJ mol^{-1} (*46*), $\Delta_f H$ ($Am^{V}O_2^+$, aq) = −804.3 ± 5.4 kJ mol^{-1} (*45*), $\Delta_f H$ (NO^+, aq) = 53.6 kJ mol^{-1} (*46*), and the enthalpy for Am^{III} complexation with nitrate $\Delta_r H = 2.0 \pm 0.5$ kJ mol^{-1} (*33*) as shown in Fig. 1C. The other is a stepwise Am-O bond formation mechanism mediated by tetravalent americium

$$Am^{III}NO_3^{2+} \xrightarrow{mh\nu} Am^{IV}O^{2+} + NO_2 (m = 2 \text{ or } 3) \quad (3)$$

$$Am^{IV}O^{2+} + H_2O \rightarrow Am^{V}O_2^{+} + H_2^{+} \quad (4)$$

$$2NO_2 + H_2O \rightarrow HNO_2 + HNO_3 \quad (5)$$

However, to our knowledge, there is no report observing the intermediate $Am^{IV}O^{2+}$, implying that the stepwise mechanism would be energetically unfavorable.

Electronic structure theory of reaction 1 is discussed below. The f-f transition at 503 nm excites trivalent americium from its electronic ground state, $^7F_0$, to the $^5L_6$ state, in which one 5f orbital is doubly occupied, four are singly occupied, and two are vacant, as shown in the electronic configuration diagrams in Fig. 1C. Subsequent f-d transition from the doubly occupied 5f orbital forms the ground state of tetravalent americium Am^{IV} ($^6H_{5/2}$) accompanied by a singly

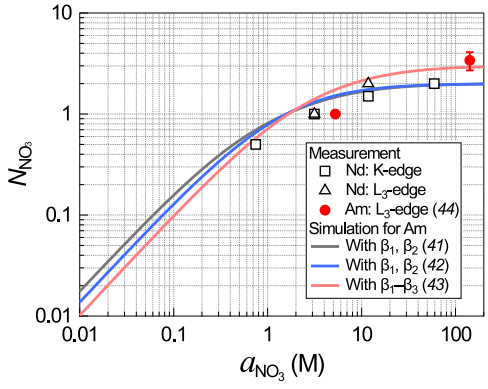

Fig. 8. Nitrate activity dependence of the average number of coordinated nitrates. Each of the three curves represents the stability constants used for the fit shown in Fig. 5. Two of them were calculated using the two-step complexation mechanism (*41*, *42*), and the other was calculated with the three-step mechanism (*43*). The number of coordinated nitrates estimated from EXAFS analyses is plotted to compare with the three curves. The red-filled circle stands for the data from americium L_3-edge EXAFS (*44*), the black open triangle stands for neodymium L_3-edge EXAFS, and the black open rectangular stands for neodymium K-edge EXAFS.

occupied 6d orbital. Furthermore, if the second f-d transition occurs from the tetravalent state in the core, then the ground state of isolated pentavalent americium ($^5I_4$) with a doubly occupied 6d orbital can be formed.

Given that americium coordinates to a nitrate, charge transfer can occur from the 6d orbital to the vacant orbital of the nitrate. As was revealed by EXAFS analyses performed by Ferrier *et al.* (*44*) and in the present study (Fig. 7 and fig. S2), two oxygen atoms symmetrically contact the americium through bidentate coordination. This fact indicates that the charge transfer from the 6d orbital can form $Am^{V}O_2^+$ and NO^+ straightforwardly as shown in the reaction diagram in Fig. 1C. If the charge transfer occurs without the second f-d transition, then electronic configuration must be changed at an avoided crossing in the course of bond rearrangement to form the pentavalent americium. The above speculation is further investigated by excited-state calculations described below.

The interaction between americium and nitrate was examined through density functional theory (DFT) calculations. First, the most stable structure of the one-nitrate complex, $Am^{III}NO_3^{2+}$, was obtained by geometry optimization. Then, molecular orbitals for the alpha spin were visualized by isosurface plots with an isovalue of 0.02 (fig. S3) with an orbital energy diagram for both alpha and beta orbitals. The index for each orbital is numbered from the 31st orbital in order of orbital energy because the lowest 30 orbitals were treated as the effective core potential.

Each of the orbitals 26 to 31 mainly consists in one of the americium 5f orbitals and is singly occupied by an alpha spin, indicating that the calculated state is the electronically ground trivalent state for americium $^7F_0$, because the spin multiplicity of septet state, which arises from the electronic configuration in the 5f orbitals in core, should not be altered by a simple coordination with a nitrate. In other words, stabilization energy gained by a long-range metal-ligand coordination should not be enough to compensate for energetical instability caused by the spin flipping among degenerate orbitals. This consideration is supported in later calculations by some spin-flipped excited states of the coordination complex. The lowest two vacant orbitals (orbitals 36 and 37) are attributed to the americium 5f and 7s (+ 6d) orbitals, respectively. In addition to this 7s + 6d orbital, other 6d-containing orbitals, 37 to 40, are thought to be candidates as a destination of the f-d transition following the initial f-f transition. Although all these orbitals can participate in the charge transfer as long as the symmetry allows that, we choose orbital 37 to theoretically elucidate a possible pathway of the charge transfer just for the feasibility reason in the following excited-state calculation. For example, orbital 38 having 6d–p* character may induce charge transfer to the p* orbital of the ligand NO_3^-. However, such a calculation has to be carried out in a lower symmetry with a larger active space because of the difference in state symmetry between the photoexcited state and the final products. We cannot handle it well with present computational resources.

To evaluate the reliability of these calculations, we compared some of the theoretical and experimental internuclear distances. As the most adequate experimental values for this purpose, we chose those obtained from EXAFS measurements of americium nitrate complex in 16 M HNO_3 (*44*). Although they reported the complex composition of $Am(H_2O)_{5.4\pm0.5}(NO_3)_{3.4\pm0.7}$, we could not find any stable structures of $Am(H_2O)_5(NO_3)_3$. Thus, that of $Am(H_2O)_4(NO_3)_3$ was adopted for the comparison. The geometry optimization was performed at the same level of theory as described above, except that we used a split valence basis set with polarization functions and a diffuse function (D95V*$^+$) on the hydrogen atom to appropriately describe hydrogen bonds. The calculated internuclear distances are listed in table S3. The theoretical and experimental values are in good agreement, indicating the reliability of the calculation regarding the interaction strength between americium and nitrate. Some of the optimized structures are drawn in Fig. 5.

To discuss the primary process that occurs immediately after the photoexcitation, it is useful to watch the number of 5f electrons. In particular, the initial $Am^{III}NO_3^{2+}$ has six 5f electrons, and the final $Am^{V}O_2^+$ has four. Two-photon excitation from the ground state causes an f-d transition of a single electron via the $^5L_6$ state, followed by charge transfer to form tetravalent americium, which has five 5f electrons. Therefore, formation of the pentavalent state requires another f-d transition. Such a transition may be achieved either by further photoexcitation or by spontaneous electron transfer triggered by bond rearrangement in the complex, that is, sudden change of electronic state at a crossing seam on the potential energy surface (PES). To assess which process is more likely, further photoexcitation or spontaneous electron transfer, we performed ab initio molecular orbital theory calculations on a five-atom system composing $AmNO_3^{2+}$ by constructing PES in an excited state correlating to $Am^{V}O_2^+ + NO^+$ and by evaluating vertical excitation energies up to the double f-d transitions.

As a result of the excited-state calculation, we found one well and two dissociation channels on the adiabatic surface in the lowest $^5A_1$ state (Fig. 9A). On the basis of the optimized value of x_{Am} (see the "Excited-state calculations" section in Materials and Methods for definition) at each grid point (Fig. 9B), the well is assigned to the Am-NO_3 bidentate coordination complex. The upper valley is assigned to the dissociation channel giving linear $AmO_2^+ + NO^+$ and the lower to bend $AmO_2^+ + NO^+$. In contrast, r_{NO} is found to exhibit small variation with r_{NO} = 1 to 1.1 Å all over the range examined here. In Fig. 9B, there are two "fault" lines accompanied by a sudden change in x_{Am}, implying changes of electronic state. To visualize the change of the electronic state more clearly, an image plot of the

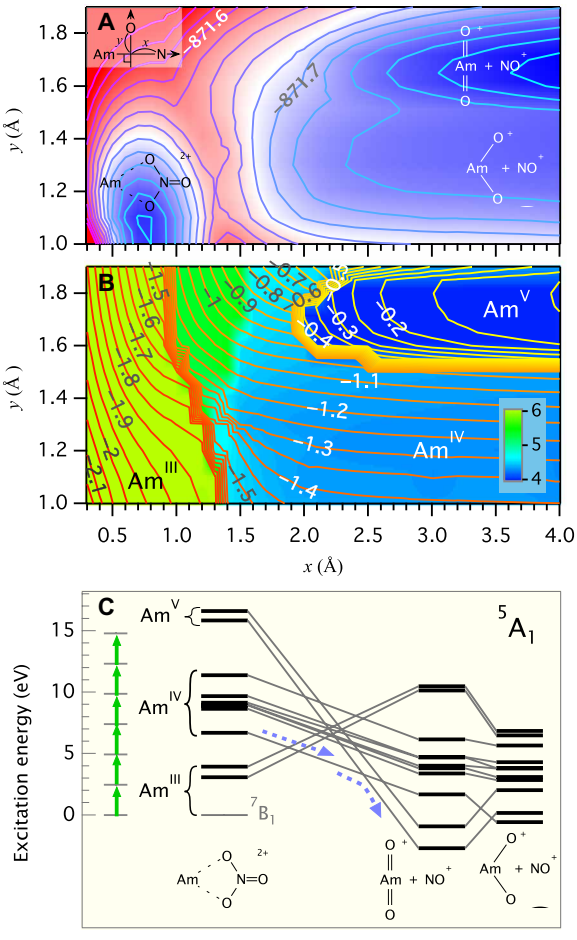

Fig. 9. Potential energy surface, change of electronic character, and correlation diagram. (**A**) Adiabatic potential energy surface of the lowest $^5A_1$ state of the $AmNO_3$ system in the C_{2v} symmetry. Total energy at each grid point is calculated by a relaxed scan at the CASSCF(6,6) level of theory. The inset presents the definition of the coordinate system. (**B**) Contour plot of the position of Am and image plot of the number of 5f electrons. (**C**) Excitation energies and correlation diagram of 11 $^5A_1$ states of the three primary structures and the ground $^7B_1$ state of the coordination complex. The gray arrows in the left-hand side indicate photon energy at 503 nm. The purple dashed arrows present the reaction path expected after the photoexcitation.

number of 5f electrons calculated at each grid point is superimposed in Fig. 9B, where the left region has six f electrons, i.e., trivalent americium, and the upper valley in the right region has four, i.e., pentavalent americium. These plots apparently indicate that the well in Fig. 9A corresponds to $Am^{III}NO_3^{2+}$, the upper valley to linear $Am^{V}O_2^{+}$, and the lower valley to bent $Am^{IV}O_2^{+}$. The fault lines in Fig. 9B reveals crossing seam, where electronic transitions between 5f and 6d orbitals occur.

In Fig. 9C, the vertical excitation energies are depicted for three different structures. We found that two- or three-photon excitation from the ground state complex gives the lowest tetravalent state. This result reasonably agrees with the experimental observation that f-d transitions occur around 5 eV. In contrast, double excitation to generate pentavalent states is denied energetically because of the too large excitation energy required. Connecting lines, which are drawn by accounting for the number of f electrons and electronic configuration for each state, present diabatic correlation between excited states. Namely, wave packets would propagate along the lines if the propagation is rapid enough to keep its electronic state without giving a chance for changing its electronic state. In the lowest $^5A_1$ state, the complex was found to adiabatically correlate with linear $Am^{V}O_2^{+}$ via two crossing points and the intermediate tetravalent state in between. This observation agrees with the feature shown in Fig. 9 (A and B). The wave packet created on the first tetravalent state by two- or three-photon excitation would propagate through the first crossing point diabatically without changing its electronic state and undergo the second crossing point adiabatically to change the electronic state to the pentavalent state. It is possible that a part of the wave packet that does not encounter the second crossing seam in Fig. 9B goes to the bent $Am^{IV}O_2^{+}$.

The present calculation does not include spin-orbit coupling. Inclusion of spin-orbit coupling may change energetics substantially. However, the existence of a reaction pathway itself should be supported by this calculation.

The tetravalent state is expected to exist as a product because there is a barrier between the two dissociation channels. However, the electronic character of the tetravalent state is strongly contaminated through a superposition with many different electronic configurations. This state may be converted to the pentavalent state with weak perturbation.

Hydration in the actual system may affect excited states via dipole interaction of OH bond and repulsion of oxygen p electrons. According to our geometry optimization of the hydrated complex of $Am^{III}(H_2O)_7NO_3^{2+}$, the lowest and the second-lowest vacant orbitals have the same irreducible representation and order in energy level as the simple model without hydration. Therefore, at least in the active space, the same behavior in the electronic state can be expected.

Although we focused on the scientific significance of the fundamental photochemical process, we briefly discuss the engineering feasibility to predict to what extent we can expect the throughput of the present laser process as an ideal case. Throughput is directly calculated as a product of the rate constant, concentration, sample volume, and atomic weight, yielding 8.4×10^{-13} kg s^{-1} for the present 10-Hz, 30-mJ laser with 2-mm spot diameter. Notably, ~85% of photons are transmitted and discarded in the present geometry. The throughput is also proportional to the laser power at a constant fluence. Therefore, using a single 1-kHz, 3-J laser with recycling discarded photons, we can treat 1.7 kg of americium per year at most. Moreover, if the fluence can be increased beyond the maximum value applied here without inducing breakdown, the throughput can increase further, as the exponent is greater than 1. The maximum amount of americium estimated here is about two orders of magnitude smaller than the inventory of the Rokkasho reprocessing plant in Japan (420 kg $year^{-1}$) (*47*), indicating that further improvement in efficiency is desired to industrialize this method; otherwise, hundreds of laser systems will be required. The above estimation helps recognize the potential of the photochemical process in real processes.

In this study, we found that trivalent americium is oxidized by multiphoton absorption at 503 nm. The photoexcitation promotes charge transfer from americium to coordinated nitrates to form pentavalent americium ($Am^{V}O_2^{+}$). This process is the first example of a resonance-enhanced photochemical process involving actinides. It gives another option for the mutual separation of f-block elements, which plays an important role in nuclear waste management. It applies also to a benchmark for actinide purification owing to its intrinsically high selectivity.

MATERIALS AND METHODS

Materials

A stock solution of americium-243 was prepared by fuming a solid mixture of americium oxide and graphite (*48*) with perchloric acid ($HClO_4$) and dissolving it in 0.1 M nitric acid (HNO_3) solution. $HClO_4$ (70%; KOSO Chemical), HNO_3 (60%; FUJIFILM Wako Pure Chemical), praseodymium(III) nitrate hexahydrate $Pr^{III}(NO_3)_3\ 6H_2O$ (>99.99%; Sigma-Aldrich), and dodecane (≥99%; Wako Pure Chemical) were used without further purification. $HClO_4$ and HNO_3 were diluted with distilled water. TODGA was used as an extractant.

Experimental methods

Am^{III} stock solution and dilute nitric acid were poured into screw-cap quartz cuvettes using micropipettes to prepare 0.4 mM Am^{III} in 0.01, 0.1, 3, and 12 M HNO_3 solutions. The cuvettes were sealed and gently shaken. The sample volume in a cuvette was 2 × 5.2 × 10 mm3 with an optical path length of 10 mm. Identification and quantitative determination were performed using a UV/vis (visible) spectrophotometer (JASCO V-670) with a spectral resolution of 1.0 or 0.2 nm. The typical absorbance at 503 nm was measured as 0.15. A nanosecond optical parametric oscillator (OPO) laser (~5 ns, <34 mJ, 10 Hz; EKSPLA NT342B) was used to excite Am^{III} with a typical irradiation time of 10 to 40 min at room temperature. The experimental setup is schematically depicted in fig. S4. The image of the laser beam profile in the OPO crystal was relayed into the cuvette with a reduction ratio of 1/3 with a relay lens of focal length f = 0.75 m, resulting in a beam diameter of 2 mm at the cuvette. The laser pulse energy was measured using a power detector (Gentec Electro-Optics, UP19K-30H-VH) coupled to a power monitor (Gentec Electro-Optics, TPM-300-CE). To measure changes in the concentrations of Am^{III} and $Am^{V}O_2^{+}$, UV/vis spectra were recorded before and after irradiation. In the separation demonstration, a solution (0.1 ml) of 0.1 mM Am^{III} and 0.55 mM Pr^{III} in 3 M HNO_3 in a cuvette was irradiated for 15 hours at 503 nm. The irradiated solution was transferred to a 2-ml glass vial with a glass Pasteur pipette. We added 16 mM TODGA in dodecane (0.1 ml) to the irradiated solution to extract Am^{III} and Pr^{III} from the aqueous phase to the organic phase. The sample solution was vigorously shaken for 20 min. After being shaken, the solution was transferred into a screw-cap quartz cuvette (optical path length, 10 mm; width, 2 mm) with a micropipette and then was centrifuged before UV/vis analysis for the aqueous and organic phases. The reason why we chose Pr^{III} as a counterpart of the separation demonstration is that, in general, molar absorption coefficients of lanthanides are an order of magnitude smaller than those of actinides (Fig. 1, A and B). We used praseodymium, whose molar absorption coefficient is the largest among lanthanides, to obtain initial concentrations as close as possible.

Pseudo–first-order rate constant

In aqueous nitric acid solution, trivalent americium exists as complexes coordinated with water and nitrate molecules. Since the photoredox reaction of metal ions is affected by the chemical environment, ligand composition is important in analyzing the reaction rate. In this context, we considered a model including stepwise complexations and photooxidations from respective complexes, as shown in Fig. 6. In this figure, we omit water molecules for simplicity and focus on the oxidation to form pentavalent americium by abstracting two oxygen anions from nitrates. The specific rate constant k_n (n = 0, 1, 2, 3, ⋯) describes a pseudo–first-order decay for each complex along a discrete-time base, which is discretized by a single cycle of the laser pulse train. In other words, k_n is approximately equal to the duty cycle (~5×10^{-8}) times the continuous-time rate constant to be observed in the presence of an electromagnetic field of the laser pulse. To monitor the change in concentration, we considered the area of the 503-nm peak, $S^{III}(t)$, which represents the total concentration of all complexes

$$c(t) = \sum_n c_n(t) \tag{6}$$

where $c_n(t)$ is the concentration of the specific complex $Am^{III}(NO_3)_n^{(3-n)}$. Assuming that the ligand substitution (all equilibrium reactions in Fig. 6) is much faster than the photooxidation, the fraction of each complex is constant with time

$$f_n = c_n(t)/c(t) \tag{7}$$

Therefore, the overall rate constant can be expressed as

$$k^{III} = \sum_n f_n k_n \tag{8}$$

Thus, the temporal variation of $c(t)$ shows a first-order decay with the rate constant k^{III}. When the laser irradiation time T is short enough for the total oxidation ratio to be much smaller than one, the decay curve is approximated by a line as

$$c(T) = c(0)\ (1 - k^{III} T) \tag{9}$$

Because $c(t)$ can be substituted with $S^{III}(t)$ in Eq. 9, we obtain the following relation

$$k^{III} = [1 - S^{III}(T)/S^{III}(0)]/T \tag{10}$$

As a result, we can determine k^{III} from $S^{III}(t)$ measured before and after laser irradiation using Eq. 10.

In addition to the overall rate constant, some specific rate constants can be estimated from the dependence of k^{III} on the nitrate activity a_{NO3}. The analytical expression of activity dependence $k^{III}(a_{NO3})$ is derived from Eq. 8 by substituting f_n with $f_n(a_{NO3})$, which is obtained by solving a simultaneous equation consisting of the definition of equilibrium constants K_n

$$k^{III}(a_{NO_3}) = \frac{k_0 + k_1\beta_1 a_{NO_3} + k_2\beta_2 {a_{NO_3}}^2 + k_3\beta_3 {a_{NO_3}}^3 + \cdots}{1 + \beta_1 a_{NO_3} + \beta_2 {a_{NO_3}}^2 + \beta_3 {a_{NO_3}}^3 + \cdots} \tag{11}$$

where $\beta_1 = K_1$, $\beta_2 = K_1K_2$, and $\beta_3 = K_1K_2K_3$. In the numerator, k_n composes the nth-order polynomial coefficient of a_{NO3}, indicating that the contribution of each k_n shows specific a_{NO3} dependence different from another. Therefore, we can estimate the relative amplitude of k_0, k_1, and k_2 from the nitrate dependence of $k^{III}(a_{NO3})$.

To evaluate the actual values of $S^{III}(t)$, the measured absorption spectra between 480 and 530 nm are fitted with a combination of functions presenting the peak profile (f_p) and the baseline (f_b) as follows

$$f_{fit}^{III}(\lambda) = f_p^{III}(\lambda) + f_b^{III}(\lambda) \tag{12}$$

We used a linear combination of three Gaussians and a linear polynomial function to replicate the peak profile and the baseline.

All 11 parameters are simultaneously adjusted in the fit. The actual value of $S^{III}(t)$ is obtained as the area of $f_p^{III}(\lambda)$. The SD of the area is calculated using the covariance matrix obtained from the fit. The fitting functions and parameters are summarized in table S4.

Typical results of the fit are shown in fig. S5 (A and C) for the spectra measured before and after laser irradiation, respectively. The absorption spectra were perfectly reproduced with nearly horizontal baselines owing to the large signal-to-noise ratio. Thus, baseline subtraction is not shown here. In fig. S5E, the filled area shows the difference between the peak profile functions obtained from the above fits. Therefore, its area represents ΔS^{III}, the difference in the peak area between $t = 0$ and T. The dots in fig. S5E indicate the difference spectrum between the measured absorption spectra. No significant discrepancy is observed between the envelope and dots for the 503-nm band.

The signal area, $S^V(t)$, for pentavalent americium is obtained in the same manner as that of the trivalent one, except for the fitting range from 700 to 735 nm. The fitting function and parameters are summarized in table S4. Notably, the position and width of the Gaussian functions are fixed during the fit. Typical results of the fit are shown in fig. S5 (B and D). In this case, the baseline is not a horizontal line but an undulating curve and could be well reproduced using a cubic function. Thus, baseline subtraction is indispensable to evaluate the signal amount shown in the lower level. The filled area represents $S^V(t)$. As shown in fig. S5F, the filled area successfully extracts signal from the scattered data.

If the observed process is only the oxidation to the pentavalent state and no other channels are involved, then ΔS^V is connected to ΔS^{III} with the ratio of the absorption coefficients at the peak wavelengths, $r_\varepsilon = \varepsilon(\lambda_p^{III})/\varepsilon(\lambda_p^V)$, and a correction factor ζ

$$\Delta S^{III} = r_\varepsilon \zeta \Delta S^V \tag{13}$$

where ζ is a factor compensating for the difference in shape between the two peaks and given by

$$\zeta = \left[\int f_p^{III}(\lambda)\, d\lambda / f_p^{III}(\lambda_p^{III})\right] \Big/ \left[\int f_p^{V}(\lambda)\, d\lambda / f_p^{V}(\lambda_p^{V})\right] \tag{14}$$

Using $\zeta = 0.55$, calculated from the fitted results, $r_\varepsilon = 7.3$ estimated from the absorption coefficients reported by Grimes *et al.* (*31*), and Eqs. 10 and 13, an empirical formula of the rate constant for the formation of pentavalent americium k^V is written by

$$k^V = 4.0 \Delta S^V / S^{III}(0) / T \tag{15}$$

Comparing k^{III} and k^V, we can determine whether the observed process is only the oxidation to form the pentavalent state.

EXAFS analysis

The above EXAFS measurements were carried out at the BL22XU at SPring-8 (8 GeV at 100 mA) at room temperature. The x-rays before and after the absorption energy of Nd K-edges were obtained by the liquid nitrogen–cooled double crystal monochromator with Si(311) for K-edge and Si(111) for L_3-edge. The EXAFS signal detection was a transmission method using ion chambers. Data acquisition was performed 32 times, and the data were used for analysis after averaging. The x-ray energy was confirmed at the inflection point of Nd K-edge as 43.576 keV using aqueous $Nd(ClO_4)_3$ solution.

For the actual procedure of the EXAFS analysis, the background removal was performed by fitting a Victoreen function (*49*) to the pre-edge and subtracting the extrapolated values. The atomic absorption was simulated using a cubic spline function divided into five regions. The extracted EXAFS oscillations were Fourier transformed in the k-space range of 3.6 to 14 $Å^{-1}$ for K-edges and 3.6 to 9 $Å^{-1}$ for L_3-edges, and fitting was performed for the spectrum converted to R-space. All the extractions and fitting processes were performed using the WinXAS3.2 program (*50*). The back-scattering factor and phase shift parameters are calculated using FEFF8.0 program (*51*). We assumed that the sum of the number of coordinated oxygens in the water-nitrate system is 9. All interatomic distances between the metal ion and oxygens of water molecules were described with a single adjustable parameter Nd-O_{H2O}. The interatomic distance between the metal ion and the contacting oxygens of the nitrate Nd-$O_{NO3,contacting}$ was calculated by adding a fixed value to Nd-O_{H2O}. The fixed value was adopted to be 0.1 Å from the previous study (*52*). The interatomic distances from the metal ion to the terminal oxygen Nd-$O_{NO3,terminal}$ and to the nitrogen Nd-N_{NO3} were treated as parameters.

DFT calculations

The interaction between americium and nitrate was examined through DFT calculations using Gaussian09 (*53*). In the calculations, we adopted the Minnesota 2006 functional (M06) (*54*), Stuttgart relativistic, small core 1997 effective core potential for americium (MWB60) (*55*), and Dunning/Huzinaga valence double-zeta basis set with polarization functions for oxygen and nitrogen (D95V*) (*56*). The reliability of the M06 functional was examined by Zhao and Truhlar (*57*).

Excited-state calculations

In the PES scan, we enforced the C_{2v} symmetry for the complex structure to focus on the simultaneous bond formation to form symmetrical AmO_2 because the bidentate structure in the nitrate coordination has been elucidated by the EXAFS analyses and the DFT calculations. This enforcement substantially reduces the number of exited states to be included and makes calculations feasible. A two-dimensional surface is constructed by relaxed scans with holding two distance parameters that are defined as the distance from the midpoint of the contacting two oxygen atoms, M, to the nitrogen atom, x, and to one of the contacting oxygen atoms, y. That is, the two-dimensional surface presents a map of the total energy optimized by varying the distance from M to the americium atom, x_{Am}, and that from the nitrogen atom to the terminal oxygen atom, r_{NO}.

We used the complete active space self-consistent field (CASSCF) calculation implemented in the OpenMolcas program package (*58*). Six active electrons are accommodated in six active orbitals denoted as CAS(6,6). The active orbitals are composed of three a_1, one b_1, one b_2, and one a_2 orbitals for the respective irreducible representations. This is the minimal active space to describe an electron transfer among trivalent, tetravalent, and pentavalent americium. To evaluate vertical excitation energies, we used the CASSCF-based second-order perturbation theory calculation implemented in the same program (*58*). For the basis set, STUTTGART_NL (*59*) for Am and ANO-L (*60*) for nitrogen and oxygen are used.

The present minimal active space can include only one 6d orbital. As the 6d orbital, we chose the lowest vacant orbital in which the main contribution is not 5f orbitals, i.e., 37 in fig. S3, which is a hybrid orbital of 7s and 6d. Note that 7s and 6d orbitals in the a_1 irreducible

representation can be mixed in the C_{2v} symmetry. Therefore, we make PES of the lowest $^5A_1$ state. Fortunately, this state is found to correlate with the ground state of the product system, $Am^VO_2^+ + NO^+$, according to a simple symmetry consideration.

Calculation of vertical excitation energies was performed at the geometry of the ground state complex $^7B_1$, which is obtained at the CASSCF(6,6) level of theory with two a_1, two b_1, one b_2, and one a_2 orbitals as the active space. This active space generates only one electronic state. In contrast, the active space for $^5A_1$ states mentioned before generates 11 states, which include 2 trivalent, 7 tetravalent, and 2 pentavalent states. For the geometry of dissociation products, we used the optimized geometry of the same five-atom system with holding only the bond distance between americium and nitrogen fixed to 10 Å.

SUPPLEMENTARY MATERIALS

Supplementary material for this article is available at https://science.org/doi/10.1126/sciadv.abn1991

REFERENCES AND NOTES

1. A. S. Kubo, D. J. Rose, Disposal of nuclear wastes. *Science* **182**, 1205–1211 (1973).
2. M. J. Hudson, L. M. Harwood, D. M. Laventine, F. W. Lewis, Use of soft heterocyclic N-donor ligands to separate actinides and lanthanides. *Inorg. Chem.* **52**, 3414–3428 (2013).
3. C. J. Dares, A. M. Lapides, B. J. Mincher, T. J. Meyer, Electrochemical oxidation of ^{243}Am(III) in nitric acid by a terpyridyl-derivatized electrode. *Science* **350**, 652–655 (2015).
4. A. V. Gelis, P. Kozak, A. T. Breshears, M. A. Brown, C. Launiere, E. L. Campbell, G. B. Hall, T. G. Levitskaia, V. E. Holfeltz, G. J. Lumetta, Closing the nuclear fuel cycle with a simplified minor actinide lanthanide separation process (ALSEP) and additive manufacturing. *Sci. Rep.* **9**, 12842 (2019).
5. T. Kooyman, Current state of partitioning and transmutation studies for advanced nuclear fuel cycles. *Ann. Nucl. Energy* **157**, 108239 (2021).
6. T. Cheisson, E. J. Schelter, Rare earth elements: Mendeleev's bane, modern marvels. *Science* **363**, 489–493 (2019).
7. R. M. Ambrosi, H. Williams, E. J. Watkinson, A. Barco, R. Mesalam, T. Crawford, C. Bicknell, P. Samara-Ratna, D. Vernon, N. Bannister, D. Ross, J. Sykes, M.-C. Perkinson, C. Burgess, C. Stroud, S. Gibson, A. Godfrey, R. G. Slater, M. J. Reece, K. Chen, K. Simpson, R. Tuley, M. Sarsfield, T. P. Tinsley, K. Stephenson, D. Freis, J.-F. Vigier, R. J. M. Konings, C. Fongarland, M. Libessart, J. Merrifield, D. P. Kramer, J. Byrne, B. Foxcroft, European radioisotope thermoelectric generators (RTGs) and radioisotope heater units (RHUs) for space science and exploration. *Space Sci. Rev.* **215**, 55 (2019).
8. W. H. Runde, B. J. Mincher, Higher oxidation states of americium: Preparation, characterization and use for separations. *Chem. Rev.* **111**, 5723–5741 (2011).
9. P. J. Panak, A. Geist, Complexation and extraction of trivalent actinides and lanthanides by triazinylpyridine *N*-donor ligands. *Chem. Rev.* **113**, 1199–1236 (2013).
10. G. J.-P. Deblonde, A. Ricano, R. J. Abergel, Ultra-selective ligand-driven separation of strategic actinides. *Nat. Commun.* **10**, 2438 (2019).
11. X.-Z. Li, L.-P. Zhou, L.-L. Yan, Y.-M. Dong, Z.-L. Bai, X.-Q. Sun, J. Diwu, S. Wang, J.-C. Bünzli, Q.-F. Sun, A supramolecular lanthanide separation approach based on multivalent cooperative enhancement of metal ion selectivity. *Nat. Commun.* **9**, 547 (2018).
12. J. A. Bogart, B. E. Cole, M. A. Boreen, C. A. Lippincott, B. C. Manor, P. J. Carroll, E. J. Schelter, Accomplishing simple, solubility-based separations of rare earth elements with complexes bearing size-sensitive molecular apertures. *Proc. Natl. Acad. Sci. U.S.A.* **113**, 14887–14892 (2016).
13. M. Simonnet, S. Suzuki, Y. Miyazaki, T. Kobayashi, K. Yokoyama, T. Yaita, Lanthanide intra-series separation by a 1,10-phenanthroline derivative: Counterion effect. *Solvent Extr. Ion Exc.* **38**, 430–440 (2020).
14. T. Donohue, Laser purification of the rare earths. *Opt. Eng.* **18**, 182181 (1979).
15. T. Donohue, Photochemical separation of elements in solution, in *Chemical and Biochemical Applications of Lasers*, C. B. Moore, Ed. (Academic Press, 1980), vol. 5, pp. 239–273.
16. D. C. Stewart, D. Kato, Analysis of rare earth mixtures by recording spectrophotometer. *Anal. Chem.* **30**, 164–172 (1958).
17. W. T. Carnall, P. R. Fields, Lanthanide and actinide absorption spectra in solution, in *Lanthanide/Actinide Chemistry*, vol. 71 of *Advances in Chemistry Series*, P. R. Fields, T. Moeller, Eds. (American Chemical Society, 1967), chap. 7, pp. 86–101.
18. W. T. Carnall, A systematic view of optical absorption spectra in the actinide series. *J. Less. Common. Met.* **122**, 1–17 (1986).
19. W. T. Carnall, A systematic analysis of the spectra of trivalent actinide chlorides in D_{3h} site symmetry. *J. Chem. Phys.* **96**, 8713–8726 (1992).
20. A. B. Yusov, V. P. Shilov, Photochemistry of f-element ions. *Russ. Chem. Bull.* **49**, 1925–1953 (2000).
21. Y. Yamada, S. Ohno, Photoreduction of solid europium chloride in KBr by visible two-photon excitation. *Chem. Lett.* **20**, 465–468 (1991).
22. M. Kusaba, N. Nakashima, Y. Izawa, C. Yamanaka, W. Kawamura, Two-photon reduction of Eu^{3+} to Eu^{2+} via the f'←f transitions in methanol. *Chem. Phys. Lett.* **221**, 407–411 (1994).
23. D. Nishida, E. Yamade, M. Kusaba, T. Yatsuhashi, N. Nakashima, Reduction of Sm^{3+} to Sm^{2+} by an intense femtosecond laser pulse in solution. *J. Phys. Chem. A* **114**, 5648–5654 (2010).
24. N. Nakashima, K. Yamanaka, T. Yatsuhashi, Reduction of Yb(III) to Yb(II) by two-color two-photon excitation. *J. Phys. Chem. A* **117**, 8352–8359 (2013).
25. L. M. Toth, J. T. Bell, H. A. Friedman, Photochemistry of the actinides, in *Actinide Separations*, vol. 117 of *ACS Symposium Series*, J. D. Navratil, W. W. Schulz, Eds. (American Chemical Society, 1980), chap. 18, pp. 253–266.
26. J. T. Bell, S. R. Buxton, Photoreduction of the uranyl ion with laser light and ethanol—I: Quantum yields and medium effects. *J. Inorg. Nucl. Chem.* **36**, 1575–1579 (1974).
27. R. Ghosh, J. A. Mondal, H. N. Ghosh, D. K. Palit, Ultrafast dynamics of the excited states of the uranyl ion in solutions. *J. Phys. Chem. A* **114**, 5263–5270 (2010).
28. S. Tsushima, Photochemical reduction of UO_2^{2+} in the presence of alcohol studied by density functional theory calculations. *Inorg. Chem.* **48**, 4856–4862 (2009).
29. T. Donohue, Photochemical separation of europium from lanthanide mixtures in aqueous solution. *J. Chem. Phys.* **67**, 5402–5404 (1977).
30. S. E. Stephanou, J. P. Nigon, R. A. Penneman, The solution absorption spectra of americium(III), (V), and (VI). *J. Chem. Phys.* **21**, 42–45 (1953).
31. T. S. Grimes, G. P. Horne, C. J. Dares, S. M. Pimblott, S. P. Mezyk, B. J. Mincher, Kinetics of the autoreduction of hexavalent americium in aqueous nitric acid. *Inorg. Chem.* **56**, 8295–8301 (2017).
32. G. Tian, D. K. Shuh, A spectrophotometric study of Am(III) complexation with nitrate in aqueous solution at elevated temperatures. *Dalton Trans.* **43**, 14565–14569 (2014).
33. P. R. Zalupski, T. S. Grimes, C. R. Heathman, D. R. Peterman, Optical absorption characteristics for $^7F_0 \rightarrow {}^5L_6$ and $^7F_0 \rightarrow {}^7F_6$ transitions of trivalent americium ion in aqueous electrolyte mixtures. *Appl. Spectrosc.* **71**, 2608–2615 (2017).
34. L. P. Varga, J. B. Mann, L. B. Asprey, M. J. Reisfeld, Calculated spectroscopic parameters and the intermediate spin-orbit coupling diagram in the interpretation of $5f^4$ AmO_2^+ spectra. *J. Chem. Phys.* **55**, 4230–4237 (1971).
35. B. J. Mincher, L. R. Martin, N. C. Schmitt, Tributylphosphate extraction behavior of bismuthate-oxidized americium. *Inorg. Chem.* **47**, 6984–6989 (2008).
36. L. P. Varga, M. J. Reisfeld, L. B. Asprey, Electronic spectra of the $5f^3$ actinides: U^{3+}, Np^{4+}, Pu^{5+}, and AmO_2^{++}. The f^3 intermediate coupling diagram. *J. Chem. Phys.* **53**, 250–255 (1970).
37. M. d. G. Gomes, S. d. S. S. Borges, L. G. F. Lopes, D. W. Franco, UV-visible spectrum of nitrous acid in solution: pK_a determination and analytical applications. *Anal. Chim. Acta* **282**, 81–85 (1993).
38. W. T. Carnall, The absorption and fluorescence spectra of rare earth ions in solution, in *Handbook on the Physics and Chemistry of Rare Earths*, K. A. Gschneidner, L. Eyring, Eds. (North-Holland Publishing Company, 1979), vol. 3, chap. 24, pp. 171–208.
39. Y. Marcus, M. Shiloh, A spectrophotometric study of trivalent actinide complexes in solution. IV. Americium with chloride ligands. *Isr. J. Chem.* **7**, 31–43 (1969).
40. W. Davis, H. J. De Bruin, New activity coefficients of 0–100 percent aqueous nitric acid. *J. Inorg. Nucl. Chem.* **26**, 1069–1083 (1964).
41. Ł. Steczek, M. Rejnis, J. Narbutt, M. C. Charbonnel, P. Moisy, On the stoichiometry and stability of americium(III) complexes with a hydrophilic SO_3–Ph–BTP ligand, studied by liquid–liquid extraction. *J. Radioanal. Nucl. Chem.* **309**, 891–897 (2016).
42. B. M. L. Bansal, S. K. Patil, H. D. Sharma, Chloride, nitrate and sulphate complexes of europium(III) and americium(III). *J. Inorg. Nucl. Chem.* **26**, 993–1000 (1964).
43. S. Andersson, C. Ekberg, J.-O. Liljenzin, M. Nilsson, G. Skarnemark, Study of nitrate complex formation with trivalent Pm, Eu, Am and Cm using a solvent extraction technique. *Radiochim. Acta* **92**, 863–867 (2004).
44. M. G. Ferrier, B. W. Stein, S. E. Bone, S. K. Cary, A. S. Ditter, S. A. Kozimor, J. S. Lezama Pacheco, V. Mocko, G. T. Seidler, The coordination chemistry of Cm^{III}, Am^{III}, and Ac^{III} in nitrate solutions: An actinide L_3-edge EXAFS study. *Chem. Sci.* **9**, 7078–7090 (2018).
45. R. J. M. Konings, L. R. Morss, J. Fuger, Thermodynamic properties of actinides and actinide compounds, in *The Chemistry of the Actinide and Transactinide Elements*, L. R. Morss, N. M. Edelstein, J. Fuger, Eds. (Springer, ed. 3, 2006), vol. 4, chap. 19, pp. 2113–2224.
46. Y. Ziouane, G. Leturcq, New modeling of nitric acid dissociation function of acidity and temperature. *ACS Omega* **3**, 6566–6576 (2018).

47. D. Albright, K. Kramer, "Neptunium 237 and americium: World inventories and proliferation concerns" (Institute for Science and International Security (ISIS) Reports, 2005).
48. T. Nishi, M. Nakada, A. Itoh, C. Suzuki, M. Hirata, M. Akabori, EXAFS and XANES studies of americium dioxide with fluorite structure. *J. Nucl. Mater.* **374**, 339–343 (2008).
49. J. A. Victoreen, The calculation of x-ray mass absorption coefficients. *J. Appl. Phys.* **20**, 1141–1147 (1949).
50. T. Ressler, WinXAS: A program for x-ray absorption spectroscopy data analysis under MS-Windows. *J. Synchrotron Radiat.* **5**, 118–122 (1998).
51. J. J. Rehr, J. J. Kas, M. P. Prange, A. P. Sorini, Y. Takimoto, F. D. Vila, *Ab initio* theory and calculations of x-ray spectra. *C. R. Phys.* **10**, 548–559 (2009).
52. T. Yaita, H. Narita, S. Suzuki, S. Tachimori, H. Motohashi, H. Shiwaku, Structural study of lanthanides(III) in aqueous nitrate and chloride solutions by EXAFS. *J. Radioanal. Nucl. Chem.* **239**, 371–375 (1999).
53. M. J. Frisch, G. W. Trucks, H. B. Schlegel, G. E. Scuseria, M. A. Robb, J. R. Cheeseman, G. Scalmani, V. Barone, B. Mennucci, G. A. Petersson, H. Nakatsuji, M. Caricato, X. Li, H. P. Hratchian, A. F. Izmaylov, J. Bloino, G. Zheng, J. L. Sonnenberg, M. Hada, M. Ehara, K. Toyota, R. Fukuda, J. Hasegawa, M. Ishida, T. Nakajima, Y. Honda, O. Kitao, H. Nakai, T. Vreven, J. A. Montgomery, J. E. Peralta, F. Ogliaro, M. Bearpark, J. J. Heyd, E. Brothers, K. N. Kudin, V. N. Staroverov, T. Keith, R. Kobayashi, J. Normand, K. Raghavachari, A. Rendell, J. C. Burant, S. S. Iyengar, J. Tomasi, M. Cossi, N. Rega, J. M. Millam, M. Klene, J. E. Knox, J. B. Cross, V. Bakken, C. Adamo, J. Jaramillo, R. Gomperts, R. E. Stratmann, O. Yazyev, A. J. Austin, R. Cammi, C. Pomelli, J. W. Ochterski, R. L. Martin, K. Morokuma, V. G. Zakrzewski, G. A. Voth, P. Salvador, J. J. Dannenberg, S. Dapprich, A. D. Daniels, Ö. Farkas, J. B. Foresman, J. V. Ortiz, J. Cioslowski, D. J. Fox, *Gaussian 09, Revision E.01* (Gaussian Inc., 2013).
54. Y. Zhao, D. G. Truhlar, The M06 suite of density functionals for main group thermochemistry, thermochemical kinetics, noncovalent interactions, excited states, and transition elements: Two new functionals and systematic testing of four M06-class functionals and 12 other functionals. *Theor. Chem. Accounts* **120**, 215–241 (2008).
55. X. Y. Cao, M. Dolg, Segmented contraction scheme for small-core actinide pseudopotential basis sets. *J. Mol. Struct. (THEOCHEM)* **673**, 203–209 (2004).
56. T. H. Dunning, P. J. Hay, Gaussian basis sets for molecular calculations, in *Methods of Electronic Structure Theory*, vol. 3 of *Modern Theoretical Chemistry*, H. F. Schaefer, Ed. (Springer, 1977), chap. 1, pp. 1–27.
57. Y. Zhao, D. G. Truhlar, Density functionals with broad applicability in chemistry. *Acc. Chem. Res.* **41**, 157–167 (2008).
58. I. F. Galván, M. Vacher, A. Alavi, C. Angeli, F. Aquilante, J. Autschbach, J. J. Bao, S. I. Bokarev, N. A. Bogdanov, R. K. Carlson, L. F. Chibotaru, J. Creutzberg, N. Dattani, M. G. Delcey, S. S. Dong, A. Dreuw, L. Freitag, L. M. Frutos, L. Gagliardi, F. Gendron, A. Giussani, L. González, G. Grell, M. Guo, C. E. Hoyer, M. Johansson, S. Keller, S. Knecht, G. Kovačević, E. Källman, G. L. Manni, M. Lundberg, Y. Ma, S. Mai, J. P. Malhado, P. Å. Malmqvist, P. Marquetand, S. A. Mewes, J. Norell, M. Olivucci, M. Oppel, Q. M. Phung, K. Pierloot, F. Plasser, M. Reiher, A. M. Sand, I. Schapiro, P. Sharma, C. J. Stein, L. K. Sørensen, D. G. Truhlar, M. Ugandi, L. Ungur, A. Valentini, S. Vancoillie, V. Veryazov, O. Weser, T. A. Wesołowski, P.-O. Widmark, S. Wouters, A. Zech, J. P. Zobel, R. Lindh, OpenMolcas: From source code to insight. *J. Chem. Theory Comput.* **15**, 5925–5964 (2019).
59. X. Cao, M. Dolg, H. Stoll, Valence basis sets for relativistic energy-consistent small-core actinide pseudopotentials. *J. Chem. Phys.* **118**, 487–496 (2003).
60. P.-O. Widmark, P.-A. Malmqvist, B. O. Roos, Density matrix averaged atomic natural orbital (ANO) basis sets for correlated molecular wave functions. *Theor. Chim. Acta* **77**, 291–306 (1990).
61. L. Abella, J. Crassous, L. Favereau, J. Autschbach, Why is the energy of the singly occupied orbital in some radicals below the highest occupied orbital energy? *Chem. Mater.* **33**, 3678–3691 (2021).

Acknowledgments: We thank S. Suzuki for preparation of americium stock solution, Y. Sasaki for synthesis of TODGA, Y. Yamada and S. Ohno for inspiring our interest, and M. Saeki for a lot of advice in laser irradiation. The radioactive materials were handled at Lab4 in Nuclear Science Research Institute of Japan Atomic Energy Agency (JAEA). The synchrotron radiation experiments were performed at BL11XU and BL22XU of SPring-8 with the approval of the Japan Synchrotron Radiation Research Institute (JASRI) (proposal nos. 2017A3504 and 2021A3711). The quantum chemistry calculations were conducted with supercomputer HPE SGI8600 in JAEA. **Funding:** This work was supported by the Japan Society for the Promotion of Science (JSPS) KAKENHI grant number JP20K19999. This work was also financially supported by an internal budget of JAEA for the Fukushima reconstruction research activity in 2020. **Author contributions:** S.M., K.Y., and T.Y. designed the experiment. S.M., K.Y., T.Y., T.K., Y.K., M.S., T.S., M.H., K.S., and R.D. prepared and performed the experiment. S.M., K.Y., and T.Y. performed the data analysis, created the figures, and wrote the manuscript. N.N. supervised the project. **Competing interests:** The authors declare that they have no competing interests. **Data and materials availability:** All data needed to evaluate the conclusions in the paper are present in the paper and/or the Supplementary Materials.

Submitted 11 November 2021
Accepted 4 April 2022
Published 18 May 2022
10.1126/sciadv.abn1991